DEVELOPMENT AND VALIDATION OF A 2D WAVE-PLASMA CODE FOR HELICON PLASMA THRUSTERS

SPACE PROPULSION 2016, ROME, ITALY / 2–6 MAY 2016

Bin Tian [(1)], Eduardo Ahedo[(1)], Mario Merino [(1)]

[(1)] Equipo de Propulsión Espacial y Plasmas (EP2), Universidad Carlos III de Madrid, Leganés, Spain, (88tian33@gmail.com)

KEYWORDS: RF Plasma Thrusters, Wave-Plasma interaction, 2D modelling

ABSTRACT:

The 2D wave-plasma interaction code (HELWAVE2D) which is specially designed for RF Plasma Thrusters is presented. The code is validated and compared against the 1D wave-plasma code (HELWAVE1D) using different simulations based on the electromagnetic field response and the power absorption of the plasma. A 2D simulation that includes the plasma plume in the magnetic nozzle of a helicon thruster is shown as a sample of the capabilities of HELWAVE2D, which will enable the analysis of the power deposition and wave loss outside of the thruster chamber.

1. INTRODUCTION

In last decades the electrodeless thrusters using a radiofrequency (RF) plasma source have raised much interest in electric propulsion [1-3]. Compared with best known types of thrusters such as ion thrusters and Hall effect thrusters, the potential merits of electrodeless thrusters would be long lifetime, simplicity of design, throttlability and compactness [4-5]. Two typical types of electrodeless thrusters are the Electron Cyclotron Resonance Thruster (ECRT) and the Helicon Plasma Thruster (HPT). Both of them are using radiofrequency waves to produce and heat a plasma in a cylindrical chamber [6]. The different frequency range used and the heating mechanisms are the principal distinction of these two thrusters. In ECRT, the energy deposition is based on the electron cyclotron resonance and therefore the radio frequency is mainly in the GHz range which can excite the microwave [7]. In comparison, a non-resonant helicon wave is mainly used to heat electrons in the HPT and the frequency is generally limited in the MHz range [8].

A typical helicon plasma thruster (shown in Fig. 1) is constituted of two main parts: a helicon source, where the plasma is generated and heated, and an external divergent magnetic nozzle, where the plasma is accelerated [5]. Based on this physical structure, four physical processes dominate in the HPT.

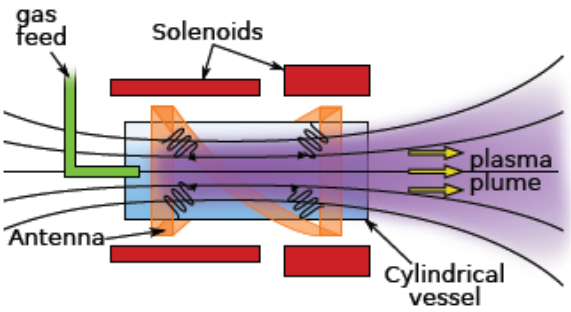

Figure 1. Sketch of the physical structure of a HPT

The wave-plasma interaction takes place inside the source leading to the deposition of wave energy into the plasma and the multiple transport phenomena governing plasma dynamics there. Two other distinguished processes take place in the magnetic nozzle (MN): the supersonic plasma acceleration and its magnetic interaction with the thruster, and the detachment from the magnetic nozzle [8]. The four main processes are coupled and influence each other. Indeed, one of the motivations for this work is the study of how and what fraction of the RF wave propagates into the MN region in HPTs and ECRTs, which could constitute a source of power inefficiency in the system.

The EP2 group is establishing a whole simulation system to describe these four processes and guide the design of Helicon Plasma Thrusters in terms of coupling and independence influence. The structure of this system is given in Fig. 2. In our previous work, the following model and code has been developed:

- The 2D (axial-radial) fluid model of the plasma source named HELFLU 2D to study plasma dynamics and transport [5].
- The 2D magnetic nozzle model DIMAGNO has been established to investigate the magnetic nozzle [9]. Moreover, DIMAGNO can be coupled with HELFLU 2D to describe the whole fluid dynamics in the HPT [10].
- Based on two fluid models, a PIC/fluid hybrid code in the plasma source and plasma plume region is being established in order to understand details in the HPT [11].

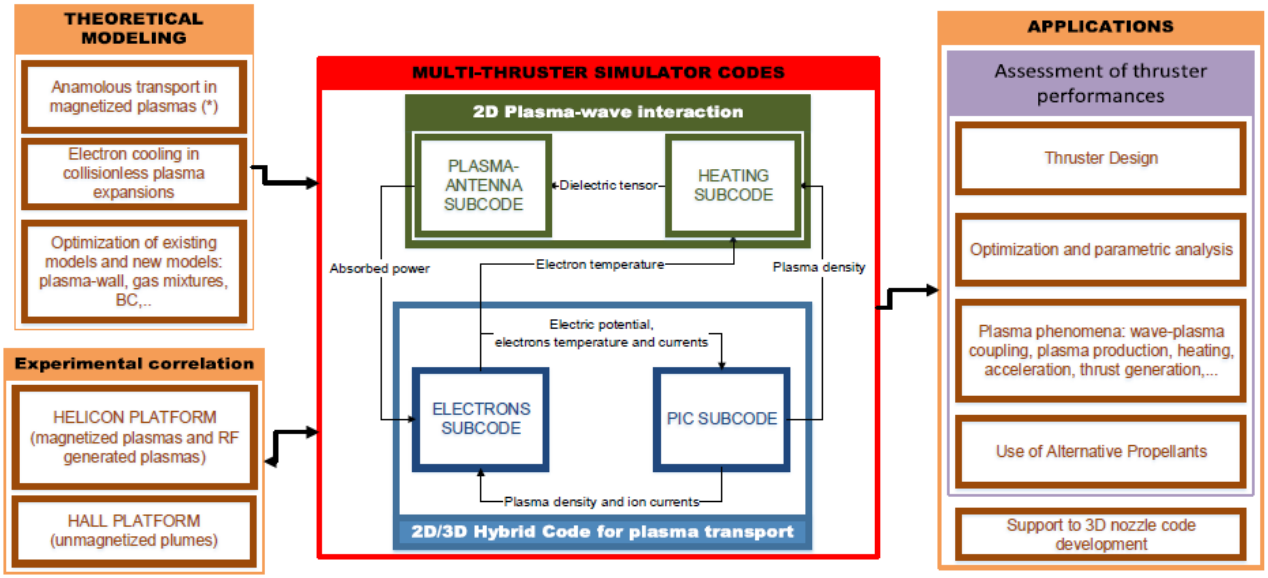

Figure 2. The model and simulation structure of HPT

- For the wave-plasma interaction, 1D cylindrical model called HELWAVE1D has been introduced in Ref. [12] to study the wave propagation and power deposition.
- Because of the non-uniformity of plasma density and magnetic field in the HPT, and the propagation of the plasma in the MN, the 1D wave-plasma code is not enough to describe the phenomena precisely. Hence, developing the 2D plasma-wave coupling model is necessary.

In this paper, the 2D wave code named HELWAVE2D is presented. This code builds upon the preliminary work of Gómez [19].

Wave-plasma interaction in the helicon source has been studied extensively in the past. In spite of this, the mechanisms of power absorption in HPT devices are not fully clear yet. Several codes both 1D and 2D have been developed by many researchers in order to study this problem. Chen and Arnush developed the 1D wave code HELIC and compared with experiment results [13]. Also, Shamrai and Cho used 1D model for the helicon source of the finite length to study the conversion of helicon and TG mode and the plasma resistance for different density profiles, respectively [14-15]. The 1D plasma kinetic code UFEM is described by Kamenski and the thickness of antenna is taken into account [16]. The 2D code using the finite different method is developed by Guangye Chen and has been used to study the radially localized helicon wave [17].

All codes we mentioned are based on the helicon source and study a purely cylindrical plasma uniform in the axial direction. The expansion of plasma plume outside the exit can nonetheless have an important role on wave propagation and absorption. Thus, the research question to be answered by HELWAVE2D is to determine the extent and the influence of wave propagation and absorption into the MN region.

According to this consideration, the near region of plasma plume can be taken into account in our model. Section 2 will introduce the model of HELWAVE2D and geometry in details and 1D code HELWAVE1D using to validate 2D code will be introduced briefly. The results and discussion will be carried out in the Section 3. Section 3.5 presents preliminary results of a 2D simulation that includes the plasma in the MN region, using the plasma profiles obtained from the DIMAGNO code, and Section 4 presents the conclusion.

2. THEORY AND MODEL

2.1. 2D wave-plasma model

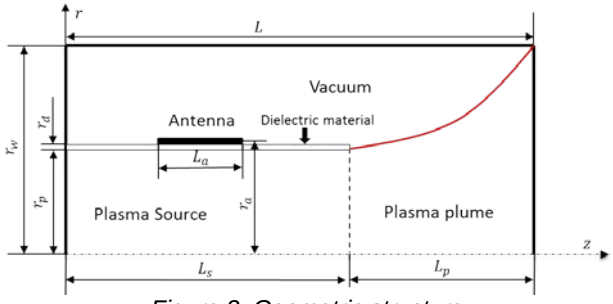

Figure 3. Geometric structure

In order to simulate the plasma-wave interaction in the helicon plasma thruster, the 2D cylindrical model is introduced here. We consider a cylindrical cavity of length L in the thruster and it includes two main parts: the plasma source of length L_s and the near region of plasma plume L_p which is shown in Fig. 3. The plasma has a fixed radius r_p is in the source part and an increasing plasma radius r_p in the region of plasma plume. Hence, the plasma

density n in the thruster is considered as a function of (r,z), $n=n(r,z)$. An rf antenna is wrapped around the plasma source and is located at $r=r_a$. The plasma is confined radially by the applied axial magnetic field $B_0(r,z)$, created by a set of external coils. The whole set is immersed in a larger conducting vessel (i.e. a Faraday cage, the vacuum chamber, etc.) of length L and radius r_w with $r_w > r_a$.

The Maxwell equations which govern the plasma-wave response of frequency ω are given in the frequency domain

$$\begin{aligned} \nabla \times \boldsymbol{E} &= i\omega \boldsymbol{B} \\ \nabla \times \boldsymbol{B} &= \mu_0(-i\omega \boldsymbol{D} + \boldsymbol{j_a}) \end{aligned} \tag{1}$$

where: $\boldsymbol{E}$ and $\boldsymbol{B}$ represent only the RF-related electromagnetic field, $\boldsymbol{j_a}$ is the external current density from the antenna. $\boldsymbol{D}$ is the electric displacement field. Fourier expansion both in time and azimuthal direction has been applied as $\exp[i(m\theta-\omega t)]$ and m is integer. Furthermore, all magnitudes are expressed in the complex form. Therefore, the Maxwell equations can be written as

$$\frac{im}{r}E_z - \frac{\partial}{\partial z}E_\theta - i\omega B_r = 0 \tag{2}$$

$$\frac{\partial}{\partial z}E_r - \frac{\partial}{\partial r}E_z - i\omega B_\theta = 0 \tag{3}$$

$$\frac{1}{r}\frac{\partial}{\partial r}(rE_\theta) - \frac{im}{r}E_r - i\omega B_z = 0 \tag{4}$$

$$\frac{im}{r}B_z - \frac{\partial}{\partial z}B_\theta + i\omega\mu_0 D_r = \mu_0 j_r \tag{5}$$

$$\frac{\partial}{\partial z}B_r - \frac{\partial}{\partial r}B_z + i\omega\mu_0 D_\theta = \mu_0 j_\theta \tag{6}$$

$$\frac{1}{r}\frac{\partial}{\partial r}(rB_\theta) - \frac{im}{r}B_r + i\omega\mu_0 D_z = \mu_0 j_z \tag{7}$$

As is known to all, the displacement field is defined as

$$\boldsymbol{D} = \bar{\bar{\epsilon}} \cdot \boldsymbol{E} \tag{8}$$

where $\bar{\bar{\epsilon}}$ is the dielectric tensor which has all the information including plasmas, the surrounding dielectric tube and the vacuum region. Considering the background magnetic field in the HPT is not purely axial, we assume α is the angle between the local magnetic field $B_0 = B_0(r,z)$ and the axis 1_z. Hence, the dielectric tensor in Eq. 8 can be written as [18-19]

$$\bar{\bar{\epsilon}} = \epsilon_0 \begin{pmatrix} k_1(\cos\alpha)^2 + k_3(\sin\alpha)^2 & ik_2\cos\alpha & \frac{k_3-k_1}{2}\sin 2\alpha \\ -ik_2 & k_1 & ik_2\sin\alpha \\ \frac{k_3-k_1}{2}\sin 2\alpha & -ik_2\sin\alpha & k_3(\cos\alpha)^2 + k_1(\sin\alpha)^2 \end{pmatrix} \tag{9}$$

where ϵ_0 is the permittivity in vacuum. For a cold, weakly-collisional plasma, the component of dielectric tensor takes the form in Ref. [18]

$$\begin{aligned} \mathrm{k}_1 &= 1 - \sum_j \frac{\omega_{pj}^2(\omega + i\nu_j)}{\omega\left[(\omega+i\nu_j)^2 - \omega_{cj}^2\right]}, \\ \mathrm{k}_2 &= -\sum_j \frac{e_j\omega_{cj}\omega_{pj}^2}{\omega\left[(\omega+i\nu_j)^2 - \omega_{cj}^2\right]}, \\ \mathrm{k}_3 &= 1 - \sum_j \frac{\omega_{pj}^2}{\omega(\omega+i\nu_j)^2}, \end{aligned} \tag{10}$$

where ω_{cj} and ω_{pj} are the cyclotron and electrostatic frequencies (of species $j=i,e$), ν_j is the collision frequency, and e_j is the sign of the electric charge.

Regarding the geometry of the antenna, the general expression of a thin antenna current density is

$$\boldsymbol{j}_a(\boldsymbol{r},t) = I_a\delta(r-r_a)\begin{bmatrix}\mathbf{1}_z s_z(\theta,z) \\ \mathbf{1}_\theta s_\theta(\theta,z)\end{bmatrix} \tag{11}$$

where I_a is the antenna current, s_z and s_θ are functions defining the geometry of antenna. The different type of antennas can be calculated in this model with using different geometric functions.

In order to solve the Maxwell equations, the finite difference method is taken into account. The mesh grid is established in the (r,z) plane. Thanks to the structure of the equations the staggered rectangular grid is considered as an appropriate discrete way to solve the problem [17, 20].

The ideally conducting walls surrounding the chamber yield the boundary conditions. The tangential electric fields vanish at the wall. It can be described as

$$E_r(r,0) = E_\theta(r,0) = 0 \tag{12}$$

$$E_r(r,L) = E_\theta(r,L) = 0 \tag{13}$$

$$E_\theta(r_w,0) = E_z(r_w,0) = 0 \tag{14}$$

In addition, the smooth condition is applied in the axis when $r=0$. To analyse equations, this condition depends on the different value of m, so we have [17]

$$E_z = rE_\theta = 0 \quad \text{for} \quad (m \neq 0) \tag{15}$$

$$rE_\theta = B_\theta = 0 \quad \text{for} \quad (m = 0) \tag{16}$$

By means of the finite difference method and boundary conditions, the Maxwell equations are transformed to a linear equations system of a general form $\boldsymbol{Ax} = \boldsymbol{b}$. All the fields can be obtained with solving this equation system.

2.2. 1D wave-plasma model

A 1D cylindrical RF field solver is employed to validate the 2D wave-plasma interaction code in this paper. The theoretical model has been introduced by Shamrai [14] and Cho [15] in detail. In our previous work [12], we developed this model to simulate the wave-plasma process in HPT. Here, only a brief introduction is given.

In the 1D wave-plasma model, stricter assumptions are taken into account because of its own limitation. The background magnetic field is assumed to be purely uniform in the axial direction. The plasma plume region is not included and only fixed plasma radius r_p is carried out. Moreover, the plasma density is limited to vary in the radial

direction only. Therefore, the dielectric tensor has its principal directions along the cylindrical reference frame axes:

$$\bar{\bar{\epsilon}} = \epsilon_0 \begin{bmatrix} k_1 & ik_2 & 0 \\ -ik_2 & k_1 & 0 \\ 0 & 0 & k_3 \end{bmatrix} \tag{17}$$

The major distinction with respect to the 2D code is that the solution is assumed to be periodic in z and it is Fourier-expanded also in the z direction:

$$\begin{pmatrix} E_r(r,\theta,z,t) \\ E_\theta(r,\theta,z,t) \\ B_z(r,\theta,z,t) \\ j_\theta(r,\theta,z,t) \end{pmatrix} = \sum_{l,m} \begin{pmatrix} E_r^{(l,m)} \\ E_\theta^{(l,m)} \\ B_z^{(l,m)} \\ j_\theta^{(l,m)} \end{pmatrix} \sin\left(\frac{l\pi}{L}z\right) \exp[i(m\theta - \omega t)], \tag{18}$$

$$\begin{pmatrix} B_r(r,\theta,z,t) \\ B_\theta(r,\theta,z,t) \\ E_z(r,\theta,z,t) \\ j_z(r,\theta,z,t) \end{pmatrix} = \sum_{l,m} \begin{pmatrix} B_r^{(l,m)} \\ B_\theta^{(l,m)} \\ E_z^{(l,m)} \\ j_z^{(l,m)} \end{pmatrix} \cos\left(\frac{l\pi}{L}z\right) \exp[i(m\theta - \omega t)], \tag{19}$$

where $k_l = l\pi/L$ is the parallel wavenumber; m is an integer and l is a positive integer.

Then, we introduce dimensionless variables,

$$\hat{k}_l = \frac{l\pi c}{L\omega}, \quad \hat{r} = \frac{r\omega}{c}, \quad \hat{\boldsymbol{B}} = \frac{\boldsymbol{B} r_a}{\mu_0 I_a}, \quad \hat{\boldsymbol{E}} = \frac{\boldsymbol{E} r_a}{\mu_0 I_a c}, \quad \hat{\boldsymbol{j}} = \frac{\boldsymbol{j} r_a c}{I_a \omega} \tag{20}$$

Substituting the field expressions and external current into Maxwell equations four differential equations and two algebraic linear equations are easily derived.

$$\frac{d\hat{E}_\phi}{d\hat{r}} = \left(\frac{\epsilon_2 m}{\epsilon_1 \hat{r}} - \frac{1}{\hat{r}}\right)\hat{E}_\phi + \frac{\hat{k}_l m}{\epsilon_1 \hat{r}}\hat{B}_\phi + \left(1 - \frac{m^2}{\hat{r}^2 \epsilon_1}\right)\hat{B}_z \tag{21}$$

$$\frac{d\hat{E}_z}{d\hat{r}} = \frac{\epsilon_2 \hat{k}_l}{\epsilon_1}\hat{E}_\phi + \left(\frac{\hat{k}_l^2}{\epsilon_1} - 1\right)\hat{B}_\phi - \frac{\hat{k}_l m}{\epsilon_1 \hat{r}}\hat{B}_z \tag{22}$$

$$\frac{d\hat{B}_\phi}{d\hat{r}} = \frac{\hat{k}_l m}{\hat{r}}\hat{E}_\phi + \left(\epsilon_3 - \frac{m^2}{\hat{r}^2}\right)\hat{E}_z - \frac{1}{\hat{r}}\hat{B}_\phi \tag{23}$$

$$\frac{d\hat{B}_z}{d\hat{r}} = \left(\frac{\epsilon_2^2}{\epsilon_1} + \hat{k}_l^2 - \epsilon_1\right)\hat{E}_\phi - \frac{\hat{k}_l m}{\hat{r}}\hat{E}_z + \frac{\epsilon_2 \hat{k}_l}{\epsilon_1}\hat{B}_\phi - \frac{\epsilon_2 m}{\epsilon_1 \hat{r}}\hat{B}_z \tag{24}$$

$$\hat{E}_r = \frac{\epsilon_2}{\epsilon_1}\hat{E}_\phi + \frac{\hat{k}_l}{\epsilon_1}\hat{B}_\phi - \frac{m}{\hat{r}\epsilon_1}\hat{B}_z \tag{25}$$

$$\hat{B}_r = \frac{m}{\hat{r}}\hat{E}_z - \hat{k}_l \hat{E}_\phi \tag{26}$$

where $\hat{E}_\phi = -i\hat{E}_\theta$, $\hat{B}_\phi = i\hat{B}_\theta$ and superscripts l, m have been omitted from the variables.

This set of equations can be solved numerically as an ordinary differential problem in radially uniform and non-uniform plasma density cases. And for radially uniform plasma density case, the equations can also be treated analytically [14-15].

2.3. Power absorption

In this part, the power absorption in plasmas is described. According to the Joule heating law, the time-averaged power density absorbed by the plasma at a given location (r, θ, z) is

$$p_{abs}(r,\theta,z) = \frac{1}{2} Re(\boldsymbol{E}^* \cdot \bar{\bar{\sigma}} \cdot \boldsymbol{E}) \tag{27}$$

where $\bar{\bar{\sigma}} = -i\omega\bar{\bar{\epsilon}}$ is the plasma conductivity tensor.

Next, averaging over θ and z the radial distribution of power density can be defined as

$$p_{abs,r}(r) = 2\pi \int_0^L p_{abs}(r,z)dz \tag{28}$$

The total absorbed power by plasmas is the integration in the whole plasma volume

$$P_{tot} = \int_V p_{abs}(r,\theta,z)dv = \int_0^{r_p} p_{abs,r}(r) r dr. \tag{29}$$

Therefore, the plasma resistance R can be calculated once P_{tot} is determined

$$R = \frac{2P_{tot}}{I_a^2} \tag{30}$$

The plasma resistance is a vital parameter to measure the efficiency of the antenna-plasma coupling. Maximizing the resistance is proposed as a main optimization criterion for the HPT.

3. RESULTS AND DISCUSSION

In this section, the validation and characterization of 2D wave-plasma code are carried out. The validation and accuracy of this code will be discussed. The 1D wave-plasma code which has been checked extensively in the past is used to validate the 2D code.

The same simulation is set up for both codes, and therefore it is restricted to the type of simulations that the 1D code can tackle. According to the Fourier expansion of 1D and 2D model, we have the relation

$$\sum_m j_\theta^2(r,z,m)exp(im\theta) = \sum_l \sum_m j_\theta^1(r,m,l)sin\left(\frac{l\pi}{L}z\right)exp(im\theta) \tag{31}$$

$$\sum_m j_z^2(r,z,m)exp(im\theta) = \sum_l \sum_m j_z^1(r,m,l)cos\left(\frac{l\pi}{L}z\right)exp(im\theta) \tag{32}$$

where the superscript 1 and 2 express the current density in the 1D and 2D model, respectively. Selecting a given (l, m) mode, Eq. 31 and 32 can be simplified to

$$\hat{j}_\theta^2(z)\delta(r - r_a) = \hat{j}_\theta^1 sin\left(\frac{l\pi}{L}z\right)\delta(r - r_a) \tag{33}$$

$$\hat{j}_z^2(z)\delta(r - r_a) = \hat{j}_z^1 cos\left(\frac{l\pi}{L}z\right)\delta(r - r_a) \tag{34}$$

where $\hat{j}$ represents the magnitude of current density.

In order to rule out the influence antenna shape, two simple virtual antennas are used to test the code. Since the plasma response is linear, we consider current only in one component, j_θ or j_z, and only one (l,m) mode at a time. All types of antenna can be seen as the sum of these two simple antennas with multiplying coefficients. Therefore, the expression of current density for these two antennas can be written as

1. Azimuthal antenna:

$$\hat{j}_\theta^1 = I_a, \quad \hat{j}_z^1 = 0 \tag{35}$$

$$\hat{j}_\theta^2(z)\delta(r-r_a) = I_a sin\left(\frac{l\pi}{L}z\right)\delta(r-r_a), \quad \hat{j}_z^2(z)\delta(r-r_a) = 0 \tag{36}$$

2. Axial antenna:

$$\hat{j}_\theta^1 = 0, \quad \hat{j}_z^1 = I_a \tag{37}$$

$$\hat{j}_\theta^2(z)\delta(r-r_a) = 0, \quad \hat{j}_z^2(z)\delta(r-r_a) = I_a cos\left(\frac{l\pi}{L}z\right)\delta(r-r_a) \tag{38}$$

In order to test the code completely, three typical situations will be investigated, including the pure vacuum case (without plasma), the uniform plasma case (plasma density $n_0$is a constant) and the non-uniform plasma case (plasma density $n_0 = n_0(r)$). Because of the similar result obtained with these two antennas in the validating simulations, only the axial antenna case and for a particular mode is shown in the present paper.

A typical 50W helicon thruster geometry and plasma properties are considered as a nominal simulation case to carry out in both 1D and 2D codes [5, 12]. The gas used is argon and the main parameters are summarized in Table 1.

Table 1 Summary of input data for the plasma-wave interaction simulations

Parameter		Value
r_p	Plasma radius	0.01m
L	Plasma and cage axial length	0.1m
r_w	External cage radius	0.02m
B_0	Applied magnetic field	150G
T_e	Plasma temperature	10eV
n_0	Plasma density	3.8 10^{18}m^{-3}
ν_e	Plasma collision frequency	8.96 10^6s^{-1}
f_{RF}	Frequency of the RF emission	13.56MHz
r_a	Antenna loop radius	0.012m
I_0	Antenna current	1A

3.1. Discussion of code convergence

A general principle for the numerical simulation in this problem is the mesh size must be smaller than the wavelength. Hence, the convergence of the HELWAVE2D code in different mesh sizes is discussed. Three different situations are calculated with different node numbers to validate the convergence of HELWAVE2D code.

Fig. 4 shows the radial profile of the component of EM fields with the variation of node numbers in the pure vacuum case. The curve convergences when the node number (n_r, n_z) is larger than $(100,50)$. In this situation the wave field is dominated by transverse electric (TE) and transverse magnetic (TM) modes. The wavelength in vacuum is $/\omega$, much larger than the mesh size we use, therefore the speed of convergence is fast.

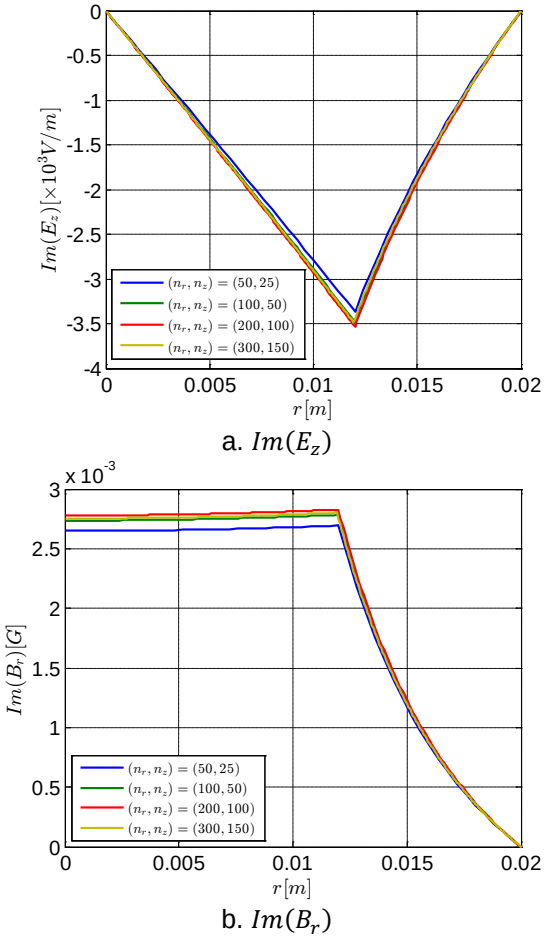

a. $Im(E_z)$

b. $Im(B_r)$

Figure 4. Convergence of wave field profiles in the pure vacuum case at $z = L/4$, $\theta = 0$ and $(l,m) = (1,1)$. Fig a and b are $Im(E_z)$ and $Im(B_r)$, respectively. (n_r, n_z) represents the node number in r and z direction, respectively.

The convergence in the uniform plasma case at different magnetic fields is demonstrated in Fig. 5 and 6. At $B_0 = 150G$, the profiles converge very quickly. However, the convergence is slow and profiles are still divergent at $B_0 = 600$. This is

because the wavelength at $B_0 = 600$ is quite small. According to the helicon plasma theory, two general modes named helicon modes and Trivelpiece–Gould (TG) mode propagates in the uniform plasma [14]. The helicon mode has a large wavelength. In comparison, the TG mode is a short wave. Increasing the magnetic field, plasmas go to the TG wave regime and the wavelength become smaller [12]. Therefore, the finer mesh grid should be taken into account in this case.

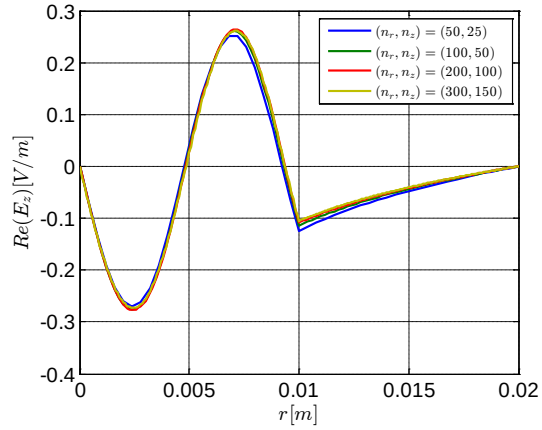

a. $Re(E_z)$

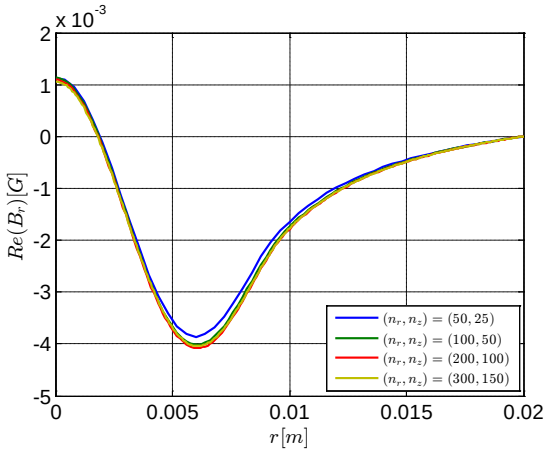

b. $Re(B_r)$

Figure 5. Convergence of wave field profiles in the uniform plasma case at $z = L/4$, $\theta = 0$ and $(l, m) = (1,1)$. The magnetic field B_0 is 150G. Fig. a and b are $Re(E_z)$ and $Re(B_r)$, respectively. (n_r, n_z) represents the node number in r and z direction, respectively.

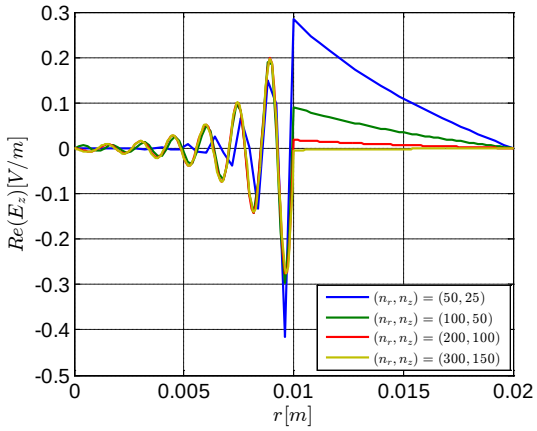

a. $Re(E_z)$

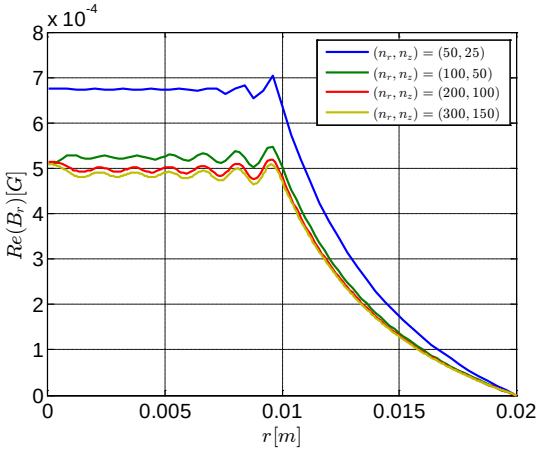

b. $Re(B_r)$

Figure 6 Convergence of wave field profiles in the uniform plasma case at $z = L/4$, $\theta = 0$ and $(l, m) = (1,1)$. The magnetic field B_0 is 600G. Fig a and b are $Re(E_z)$ and $Re(B_r)$, respectively. (n_r, n_z) represents the node number in r and z direction, respectively.

3.2. Comparison in the vacuum case

After the discussion of convergence, the validation of HELWAVE2D code is considered. HELWAVE1D code which has been proved in our previous work is chosen to compare.

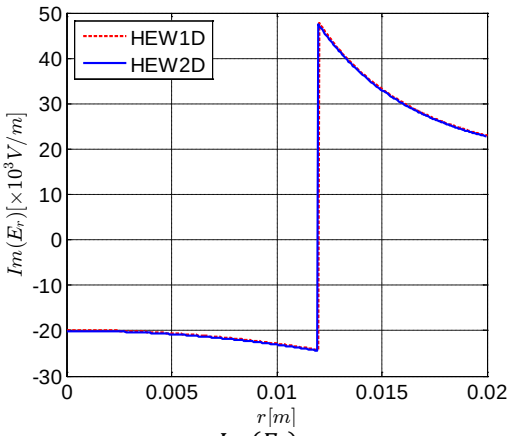

a. $Im(E_r)$

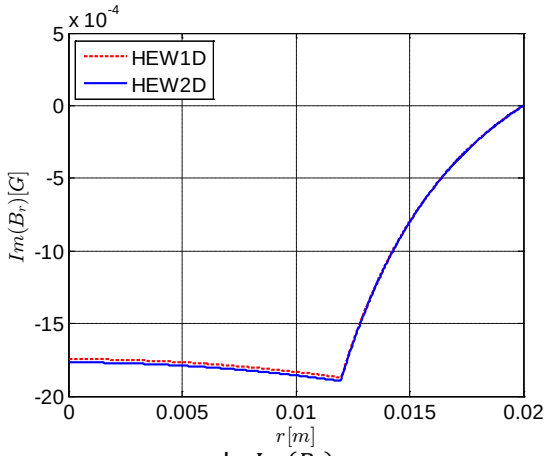

b. $Im(B_r)$

Figure 7. Comparison between HELWAVE1D and HELWAVE2D of wave field profiles in the pure vacuum case at $z = L/3$, $\theta = 0$ and $(l, m) = (2,1)$. Fig a and b are $Im(E_r)$ and $Im(B_r)$, respectively.

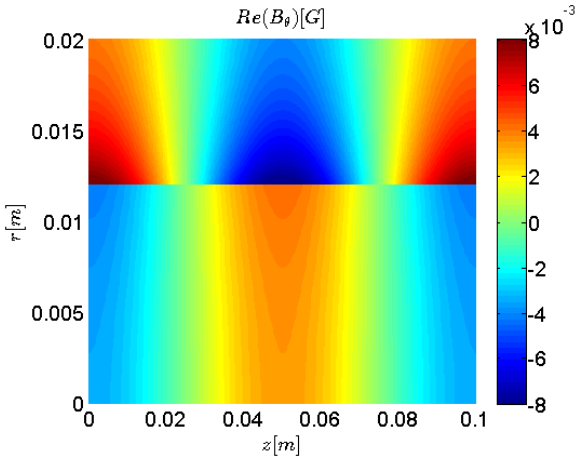

a. HELWAVE1D

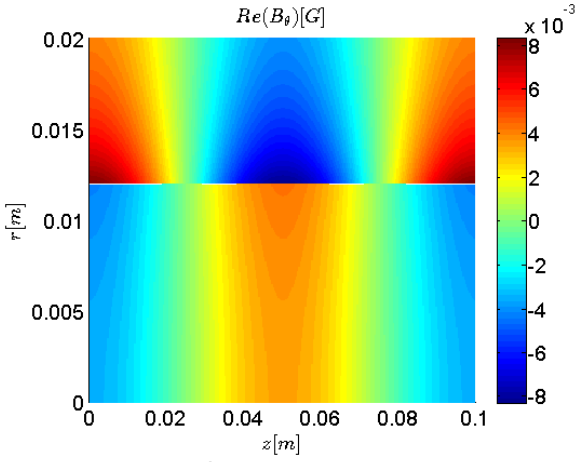

b. HELWAVE2D

Figure 8. Comparison in the pure vacuum case of 2D wave fields in both r and z direction between HELWAVE1D and HELWAVE2D code at $\theta = 0$ and $(l, m) = (2,1)$. Fig a and b are $Im(E_z)$ and $Re(B_\theta)$, respectively.

In this section, the comparison between HELWAVE1D code and HELWAVE2D code in the vacuum case is carried out. The radial distribution of wave fields is compared in Fig. 7. The results calculated by two codes are consistent. The 2D plot of the component of EM field in both r and z direction shown in Fig. 8 further confirms the consistency between the two codes.

3.3. Comparison in the uniform plasma case

Fig. 9 shows the validation in the uniform plasma at $B_0 = 150G$. The real part of E_r and B_r is compared between two codes. The harmonic behaviour of wave fields is observed. The consistency is not changed whether having plasmas or without plasmas.

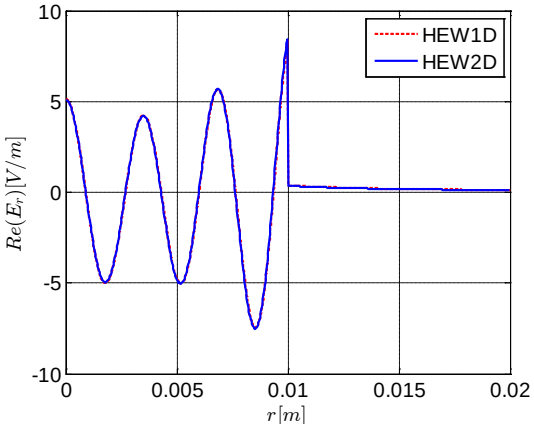

a. $Re(E_r)$

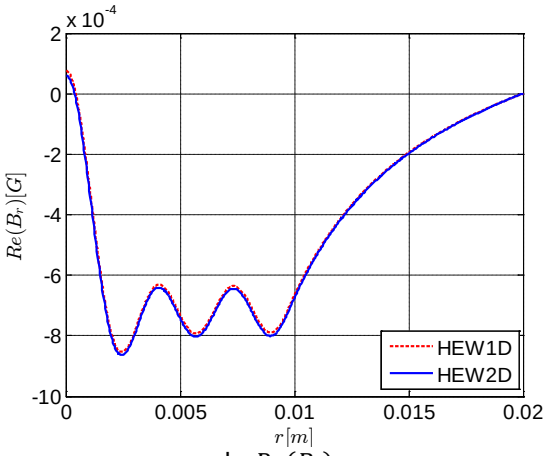

b. $Re(B_r)$

Figure 9. Comparison between HELWAVE1D and HELWAVE2D of wave field profiles in the uniform plasma case at $z = L/3$, $\theta = 0$ and $(l, m) = (2,1)$. The magnetic field B_0 is 150G. Fig a and b are $Re(E_r)$ and $Re(B_r)$, respectively.

Comparing the 2D plot in Fig. 10, the harmonic behaviour is not only in the radial direction, but also in the axial directions. Both of two codes show it clearly. The reason of this phenomenon is the influence of both helicon mode and TG mode and the cosine shape of current density.

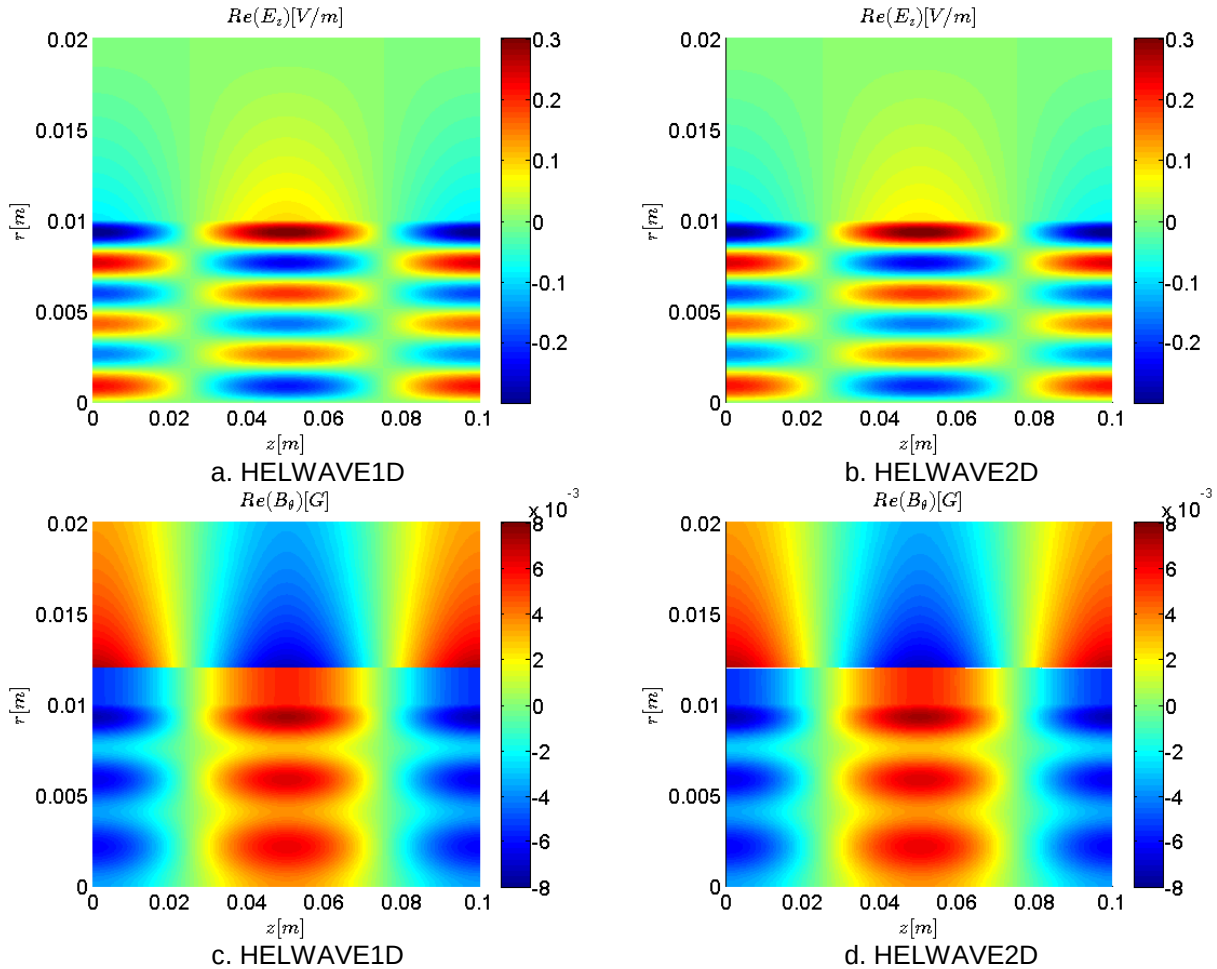

Figure 10. Comparison in the uniform plasma case of 2D wave fields in both r and z direction between HELWAVE1D and HELWAVE2D code at $\theta = 0$ and $(l, m) = (2,1)$. The magnetic field B_0 is 150G.

In order to confirm the consistency between two codes in more detail, the power deposition in plasmas is compared. The distribution of power absorption in the radial direction is given in Fig. 11. It is well consistent. The total power absorbed by plasmas and the plasma resistance is shown in Tab. 2. It further proved that the HELWAVE2D has a good accuracy and the error is less than 1%.

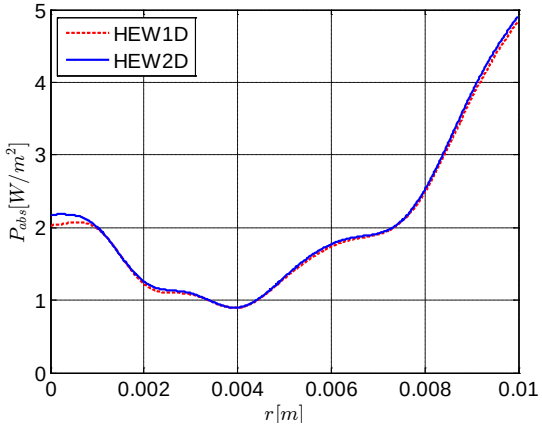

Figure 11. Comparison of the distribution of power absorption in r direction between HELWAVE1D and HELWAVE2D code in the uniform plasma case at $(l, m) = (2,1)$. The magnetic field B_0 is 150G.

Table 2 Comparison of Total power and resistance

	Total Power (W)	Resistance (Ω)
HELWAVE1D	1.192×10^{-4}	2.384×10^{-4}
HELWAVE2D	1.197×10^{-4}	2.394×10^{-4}

3.4. Comparison in the radially non-uniform plasma case

Generally, the plasma density is not uniform in the HPT. Therefore, the non-uniform plasma case is necessary to be discussed. To investigate this situation, the density profile is assumed to be given by

$$n(r) = n_0 \left[1 - \left(\frac{r}{r_p}\right)^s\right]^t \tag{39}$$

Here, $(s, t) = (2,1)$ and $(s, t) = (2,2)$ is employed to form density profiles. It is shown in Fig. 12.

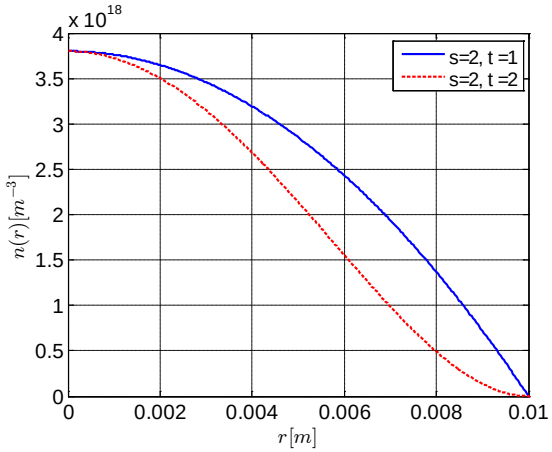

Figure 12. The density profiles

Similarly, the radial profile of wave fields and 2D plot is applied to validate the 2D code. Fig. 13- 14 are the results for $(s,t) = (2,1)$ and Fig. 15 -16 for $(s,t) = (2,1)$. For these two different density profiles, the results from HELWAVE2D are well consistent with ones from HELWAVE1D. It shows that the HELWAVE2D code is suitable for calculating complex situations.

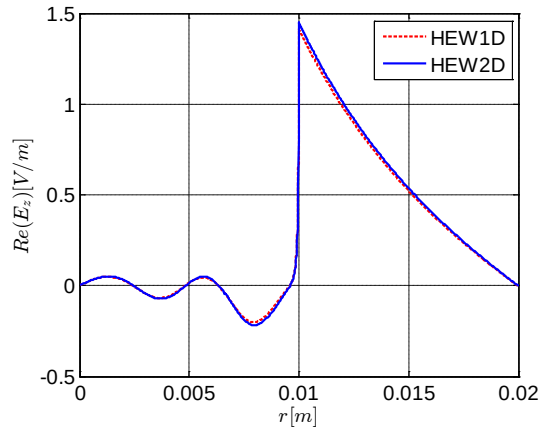

a. $Re(E_z)$

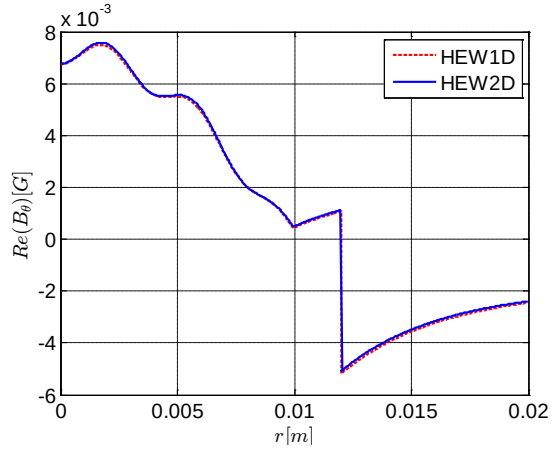

b. $Re(B_\theta)$

Figure 13. Comparison between HELWAVE1D and HELWAVE2D of wave field profiles in the non-uniform plasma case at $z = L/3$, $\theta = 0$ and $(s,t) = (2,1)$, $(l,m) = (2,1)$. The magnetic field B_0 is 150G. Fig a and b are $Re(E_z)$ and $Re(B_\theta)$, respectively.

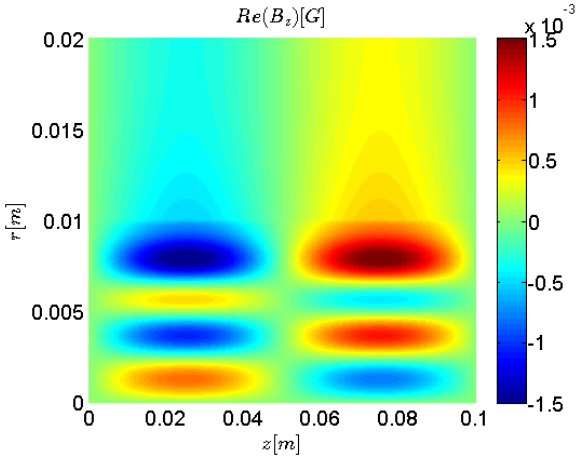

a. HELWAVE1D

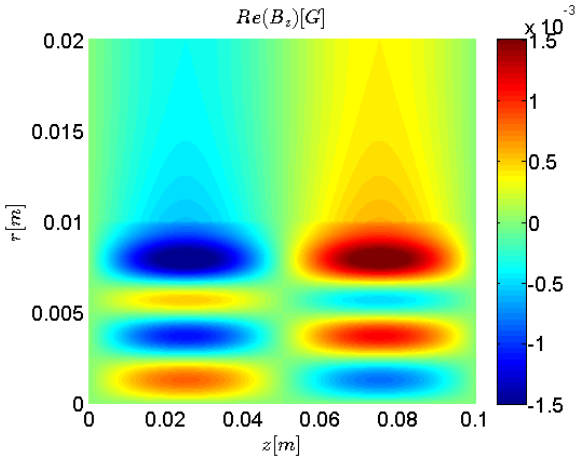

b. HELWAVE2D

Figure 14. Comparison in the non-uniform plasma case of 2D wave fields in both r and z direction between HELWAVE1D and HELWAVE2D code at $(s,t) = (2,1)$, $(l,m) = (2,1)$ and $\theta = 0$. The magnetic field B_0 is 150G.

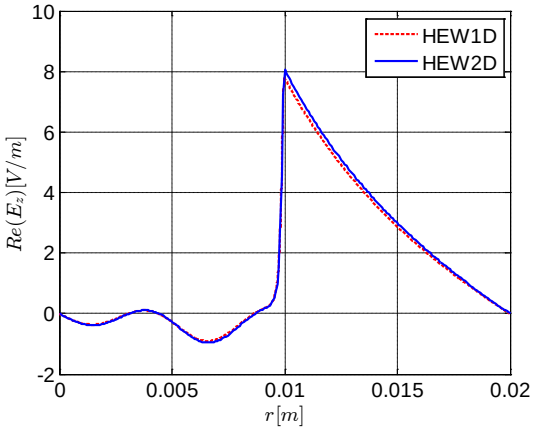

a. $Re(E_z)$

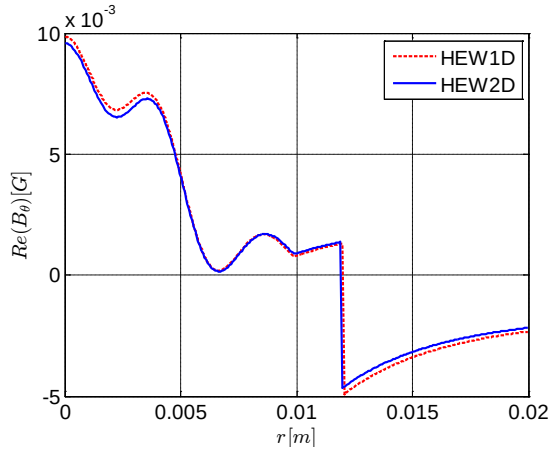

b. $Re(B_\theta)$

Figure 15. Comparison between HELWAVE1D and HELWAVE2D of wave field profiles in the non-uniform plasma case at $z = L/3$, $\theta = 0$ and $(l, m) = (2,1)$, $(s, t) = (2,2)$. The magnetic field B_0 is 150G. Fig a and b are $Re(E_z)$ and $Re(B_\theta)$, respectively.

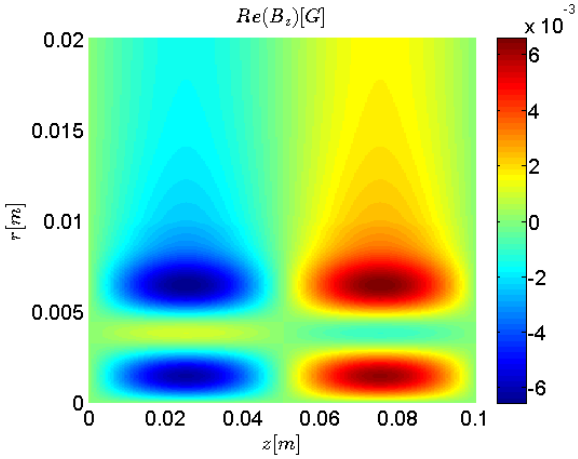

a. HELWAVE1D

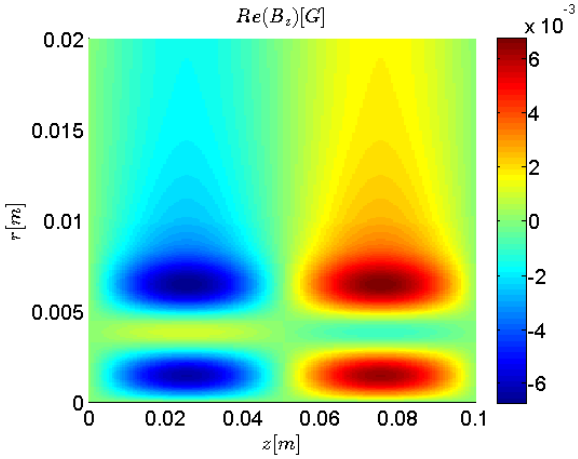

b. HELWAVE2D

Figure 16. Comparison in the non-uniform plasma case of 2D wave fields in both r and z direction between HELWAVE1D and HELWAVE2D code at $(s, t) = (2,1)$, $(l, m) = (2,1)$ and $\theta = 0$. The magnetic field B_0 is 150G.

The distribution of power absorption for two different density profiles in the radial direction is shown in Fig. 17. The power absorption concentrates near the boundary and few power deposits in the bulk region. The density profile has significant influence on the power deposition. The profile $(s, t) = (2,2)$ absorbs more power than $(s, t) = (2,1)$. Tab. 3 gives the total power and plasma resistance for these two profiles. The error between 1D and 2D code is less than 1%.

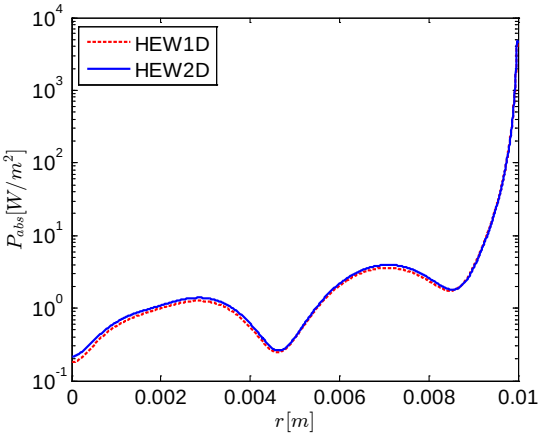

a. $(s, t) = (2,1)$

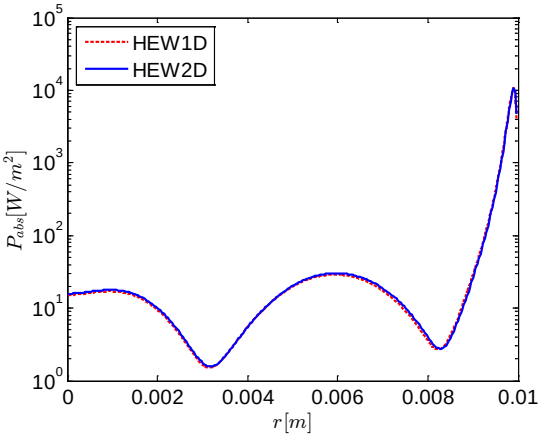

b. $(s, t) = (2,2)$

Figure 17. Comparison of the distribution of power absorption in r direction between HELWAVE1D and HELWAVE2D code in the non-uniform plasma case for $(l, m) = (2,1)$. The magnetic field B_0 is 150G. Fig a is $(s, t) = (2,1)$ and Fig b is $(s, t) = (2,2)$.

Table 3 Comparison of Total power and resistance

	$(s, t) = (2,1)$		$(s, t) = (2,2)$	
	Total Power (W)	Resistance (Ω)	Total Power (W)	Resistance (Ω)
1D	3.709×10^{-3}	7.418×10^{-3}	0.0204	0.0408
2D	3.712×10^{-3}	7.424×10^{-3}	0.0205	0.0410

3.5. A specific simulation case

In this section, a preliminary simulation case including the near region of the plasma plume in the MN is carried out by HELWAVE2D to illustrate the capabilities of the code. The plasma density and magnetic field are obtained from the MN code

DIMAGNO. A Nagoya III type antenna is used in this case. The length of the plasma source L_s is 0.05m and the plasma plume part is $L_p = 0.1$m.

Fig. 17 shows the distribution of plasma density in this simulation. The red line is the boundary of plasmas and the black box shows the antenna positions. Solid lines depict the direction of the magnetic field in the MN region.

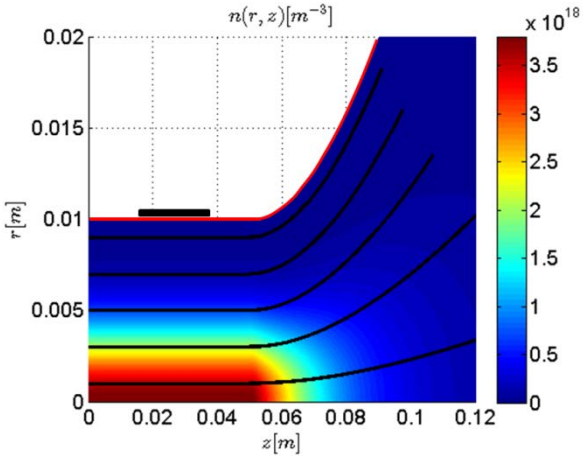

Figure 17. The 2D distribution of plasma density. The red line is boundary of plasmas. The black box shows the position of antenna. Solid lines are magnetic lines.

To reduce the direct influence of the conducting wall boundary condition used in this simulation, the last 3 cm around the perimeter of the simulation box are discarded and not shown in the plots. Future work will study non-reflective boundary conditions to better describe the actual situation in a space plasma thruster. The distribution of the component of magnetic field B_z in the chamber is given in Fig. 18. It is shown that the wave mainly propagates in the source region, where it is strongest. However, the wave can be seen to propagate also into the MN region.

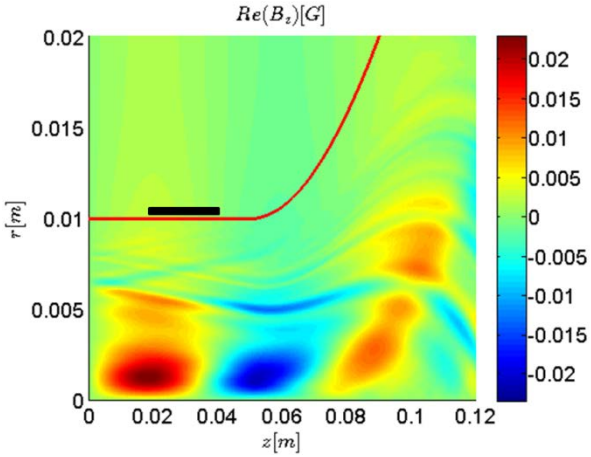

Figure 18. The 2D distribution of wave field B_z. The red line is boundary of plasmas. The black box shows the position of antenna.

Interestingly, the power absorption density in the whole chamber concentrates fundamentally in the source region (Fig. 19). This does not preclude, however, that the antenna is radiating to infinity and that this power is not absorbed in the MN region: further studies will concentrate in studying the reflection of the wave by the plasma back into the source region as the density and magnetic field strength (and consequently, the dielectric tensor) change as the plasma expands. Clearly, an efficient RF thruster will require little or no radiation to empty space and maximum absorption within the source region.

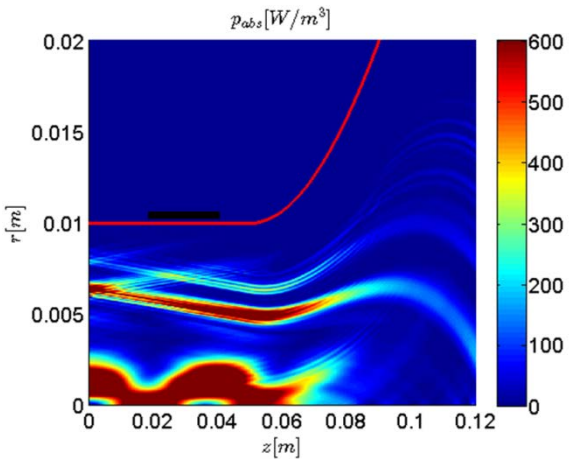

Figure 19. The 2D distribution of power density. The red line is boundary of plasmas. The black box shows the position of antenna.

4. CONCLUSION

A 2D wave-plasma interaction code named HELWAVE2D has been developed in order to study the wave propagation and power deposition in the Helicon Plasma Thrusters (HPT). The non-uniformity both in the plasma density and magnetic field in radial and axial direction is taken into account. The cold plasma dielectric tensor is employed. As a distinguishing factor from other helicon wave codes, the near region of plasma plume is included in the model. The plasma boundary can be changed along the chamber length. Based on this consideration, the finite different method is applied to solve this problem The Maxwell equations are investigated in the frequency domain and the Fourier expansion is applied in the azimuthal direction and time. A staggered mesh approach which has a good second-order accuracy and low computational cost is employed to discretize the equations.

In order to validate the code in different situations, the convergence in different conditions has been discussed. Obviously, the mesh size should be much smaller than the wavelength. According to the helicon plasma theory, the helicon mode and Trivelpiece–Gould (TG) modes are the two dominated mode. The mesh size should be finer when the TG wave (a short wave) mainly propagates in the plasma region. Moreover, the comparison to the HELWAVE1D code has been

carried out. Three different cases including pure vacuum case, uniform plasma case and non-uniform plasma case have been checked to validate the 2D code. The two codes have good consistency and the error has been proved to be less than 1%.

A preliminary simulation case including the magnetic nozzle is carried out. It shows that the wave can propagate to the downstream. Further work will concentrate on analyzing wave propagation and absorption outside of the plasma source region and in studying different boundary conditions.

5. ACKNOWLEDGMENTS

This work has been supported by the Spanish R&D National Plan, Grant No. ESP2013-41052-P. Bin Tian, also thanks the financial support provided by Chinese Scholarship Council (CSC) for his PhD studies at UC3M in Spain.

6. REFERENCES

1. West, M. D., Charles, C., & Boswell, R. W. (2008). Testing a helicon double layer thruster immersed in a space-simulation chamber. Journal of Propulsion and Power, 24(1), 134-141.

2. Pottinger, S., Lappas, V., Charles, C., & Boswell, R. (2011). Performance characterization of a helicon double layer thruster using direct thrust measurements. Journal of Physics D: Applied Physics, 44(23), 235201.

3. Pavarin, D., Ferri, F., Manente, M., Curreli, D., Guclu, Y., Melazzi, & Ahedo, E. (2009, September). Design of 50 W helicon plasma thruster. In 31st Int. Electric Propulsion Conf., Ann Arbor, MI (pp. 2009-205).

4. Ahedo, E. (2011). Plasmas for space propulsion. Plasma Physics and Controlled Fusion, 53(12), 124037.

5. Ahedo, E., & Navarro-Cavallé, J. (2013). Helicon thruster plasma modeling: Two-dimensional fluid-dynamics and propulsive performances. Physics of Plasmas (1994-present), 20(4), 043512.

6. Cannat, F., Lafleur, T., Jarrige, J., Chabert, P., Elias, P. Q., & Packan, D. (2015). Optimization of a coaxial electron cyclotron resonance plasma thruster with an analytical model. Physics of Plasmas (1994-present), 22(5), 053503.

7. Miyoshi, H., Ichimura, S., Yoshinodai, S., & Horiuchi, Y. (1991). Microwave Ion Thruster with Electron Cyclotron Resonance Discharge. energy, 91, 084.

8. Ahedo, E. (2013). Plasma dynamics in a helicon thruster. In Progress in Propulsion Physics (Vol. 4, pp. 337-354). EDP Sciences.

9. Ahedo, E., & Merino, M. (2012). Two-dimensional plasma expansion in a magnetic nozzle: Separation due to electron inertia. Physics of Plasmas (1994-present), 19(8), 083501.

10. Merino, M., & Ahedo, E. (2016). Fully magnetized plasma flow in a magnetic nozzle. Physics of Plasmas (1994-present), 23(2), 023506.

11. Merino, M., Cichocki, F., & Ahedo, E. (2015). A collisionless plasma thruster plume expansion model. Plasma Sources Science and Technology, 24(3), 035006.

12. Tian, B., Ahedo, E., & Navarro-Cavalle, J. (2014). Investigation of Plasma-wave Interaction in Helicon Antenna Thrusters. In The 50th AIAA/ASME/SAE/ASEE Joint Propulsion Conference& Exhibit, AIAA Paper (No. 2014-3475).

13. Arnush, D., & Chen, F. F. (1998). Generalized theory of helicon waves. II. Excitation and absorption. Physics of Plasmas (1994-present), 5(5), 1239-1254.

14. Shamrai, K. P., & Taranov, V. B. (1994). Resonance wave discharge and collisional energy absorption in helicon plasma source. Plasma Physics and Controlled Fusion, 36(11), 1719.

15. Cho, S., & Kwak, J. G. (1997). The effects of the density profile on the power absorption and the equilibrium density in helicon plasmas. Physics of Plasmas (1994-present), 4(11), 4167-4172.

16. Kamenski, I. V., & Borg, G. G. (1998). A 1D cylindrical kinetic wave code for helicon plasma sources. Computer physics communications, 113(1), 10-32.

17. Chen, G., Arefiev, A. V., Bengtson, R. D., Breizman, B. N., Lee, C. A., & Raja, L. L. (2006). Resonant power absorption in helicon plasma sources. Physics of Plasmas (1994-present), 13(12), 123507.

18. Stix, T. H. (1962). The theory of plasma waves. The Theory of Plasma Waves, New York: McGraw-Hill, 1962, 1.

19. Jaume, N. C. (2013). Helicon Plasma Thrusters: prototypes and advances on modeling The 33rd International Electric Propulsion Conference.

20. Yee, K. S. (1966). Numerical solution of initial boundary value problems involving Maxwell's equations in isotropic media. IEEE Trans. Antennas Propag, 14(3), 302-307.